SNR Improvement for Maneuvering Ship Using Weak Echo Under the Condition of Beidou GEO Satellites

Yan Li 🆔, Songhua Yan 🆔, and Jianya Gong

Abstract—Using global navigation satellite systems as transmitters of opportunity for target detection is a hot issue. The problems of this technology are the restricted power budget provided by navigation satellites and the defocusing caused by the movement of target. To refocus the echo and improve the signal-to-noise ratio under the condition of Beidou Geostationary satellites, this article uses jointly the short-time coherent integration and the long-time integration based on Fractional Fourier transform to correct the range migration and the Doppler frequency migration of signals for refocusing the signal energy. The effectiveness of the proposed algorithm for refocusing the echo from different types of maneuvering ships (a cargo ship and a ferry) is confirmed via an experimental campaign.

Index Terms—Beidou geostationary (GEO) satellites, global navigation satellite systems (GNSS), maneuvering ships, signal-to-noise ratio (SNR) improvement.

I. INTRODUCTION

MOTIVED by the well-known advantages of no dedicated transmitter and low cost of passive radar, researchers exerted great effort in investigating how to conduct target detection based on passive radar over the last years. Traditionally, the use of passive radar for target detection has relied predominantly on terrestrial signal sources, such as digital audio broadcasting/digital video broadcasting-terrestrial [1], [2], frequency modulation (FM) [3], [4], and global system for mobile [5]. Unfortunately, these terrestrial signal sources have limited coverage and are difficult to illuminate the blue water. Therefore, researchers turn their attention to spaceborne opportunity signal sources to increase space coverage and time continuity by using more opportunity signal sources.

Currently, the use of suitable global navigation satellite systems (GNSS) constellations, such as Galileo, global position system (GPS), GLONASS, and Beidou, as spaceborne opportunity signal sources to conduct remote-sensing detection applications has become an interesting field for researchers. GNSS signals that can be selected as the signal source to constitute a passive radar for target detection possess the following advantages. First, GNSS has a relatively large bandwidth with a maximum range resolution of 15 m (using the Galileo E5a/b signals, the GPS L5, or the Beidou B3). Second, the coverage of GNSS signal is global, including the blue water.

Beidou system is a great choice to be used as transmitters of opportunity because it has five unique geostationary (GEO) satellites. GEO satellites have stable azimuth and elevation angle (almost constant), which means that each Beidou GEO satellite has an invariable illuminating area and can provide the possibility for the long-time monitoring in a specific area.

Unfortunately, the studies on target detection based on GNSS-based passive radar, including Beidou GEO-based radar, encounter a serious challenge of weak echo [6], [7]. The main reason for the weak echo is the restricted transmitted power of GNSS constellations. For example, the minimum received power levels on the ground of the Beidou B3I signals are specified to be -163 dBw, which are measured at the output of a 0 dBi right-handed circular polarization (RHCP) user receiving antenna [8]. The restricted budget of signals may result in the interested target not being indicated in range compressed (RC) map. As a result, the SNR of echo cannot be focused by directly using integration algorithms.

On the other hand, the motion state of target, especially maneuvering target, has an influence on the energy accumulation under the condition of Beidou GEO-based radar. For maneuvering target, the echo not only has a Doppler frequency and range migration (RM) caused by initial velocity, but also has Doppler frequency migration (DFM) caused by radial acceleration [9]. If usual methods are used to compensate the Doppler and RM, the DFM cannot be solved. In long integration time, the echo of maneuvering target may be defocused by DFM, and the energy of echo cannot be integrated. Thus, the effective compensation of RM and DFM is necessary to improve the SNR of echo.

Aiming at improving the SNR of echo, researchers have investigated algorithms to improve the coherence of signals by compensating RM and DFM. The widely used moving target detection (MTD) method [10], which uses a Doppler filter bank to correct the Doppler shift within one range cell, possesses a limited performance for uniform motion target with high speed. The target's envelope may easily walk across several range cells because of the target's initial velocity and fine range resolution. This phenomenon is called the RM effect. In this case, the energy of the target is distributed in the range direction during the

integration time, and the RM problem will become worse with faster velocity. Therefore, MTD can improve SNR significantly within only a range cell. To solve the RM effect, a popular method called keystone transform (KT) is introduced to correct the RM [11]. This method involves the remapping of slow-time axis without the DFM effect. However, this method is only effective for signals with high radial velocity and relatively high bandwidth. In addition, it cannot correct the DFM caused by the radial velocity. Recently, a novel Radon–Fourier transform (RFT) is proposed to realize the long-time integration for the moving target with RM [12]–[14]. The RFT can overcome the coupling between the range walk and phase modulations effectively by jointly searching along with range and velocity directions of the moving target. Nevertheless, it will bring about the integration loss in case of the DFM. To solve the DFM problem caused by maneuvering targets, the Birmingham team proposed the target motion compensation (TMC) algorithm to compensate for the Doppler frequency [15]–[17]. The performance of TMC algorithm greatly depends on information precision. Moreover, Li *et al.* [18] proposed a SNR improvement algorithm by combining KT and fractional Fourier transform (FrFT). This algorithm can treat the target as a uniform motion in a short time by dividing the data into frames. Finally, the SNR can be improved through noncoherent integration. Although this algorithm has been verified by simulation data, it lacks the support of field experiments, and computational complexity increases with the frame amount.

To solve the restricted power budget and the motion state of target, this article proposes an energy accumulation algorithm by jointly using short-time coherent integration and long-time integration under the condition of Beidou GEO satellites. This algorithm first conducts short-time coherent integration to suppress the clutter and indicate the trajectory of target in RC map. The contribution of short-time integration is to indicate the target area in RC map and further reduce the search of the interested areas in RC map, which means that the computation of the algorithm is reduced. Then, the algorithm extracts the target's echo to correct RM and uses FrFT to eliminate the DFM effect. Moreover, the algorithm can identify the motion parameters of the target automatically. The proposed algorithm is validated by the real data.

The rest of this article is organized as follows: Section II presents the GNSS bistatic radar geometry and basic signal preprocessing (range compression). Section III illustrates the overview of common algorithms, such as MTD, RFT, and TMC. Section IV discusses the FrFT-based SNR improvement algorithm. Section V shows the cargo ship with high radar cross section (RCS) experiment and the SNR improvement results. Section VI illustrates the ferry experiment with low RCS and the improvement results. Finally, Section VII concludes this article.

II. GNSS BISTATIC RADAR GEOMETRY AND RANGE COMPRESSION

This section shows the geometry of bistatic radar based on Beidou GEO satellite and then illustrates the range compression by providing a foundation for the subsequent analysis of echo's RM and DFM.
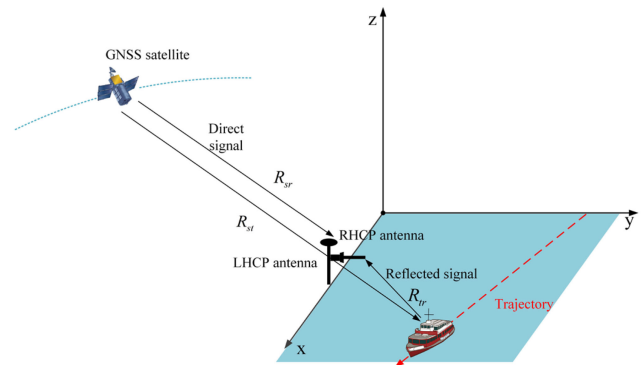

Fig. 1. GNSS-based bistatic radar system for target detection with a stationary receiver (RHCP and LHCP antennas) and a satellite.

A. GNSS Bistatic Radar Geometry

The GNSS-based geometry is shown in Fig. 1 to describe the signal model of GNSS bistatic radar that can be used for further signal processing. The illuminator of opportunity is a Beidou GEO satellite, while the stationary receiver is on the ground. The receiver consists of a RHCP antenna to receive direct signals from all available Beidou GEO satellites and a high-gain left-handed circular polarization (LHCP) antenna to receive the weak reflected signals from the interested target. The choice of LHCP antenna for radar channel is to minimize the direct path interference. Beidou GEO satellites operate in orbit at an altitude of 35786 kilometers and are located at 58.75°E, 80°E, 110.5°E, 140°E, and 160°E respectively. The B3I signal is composed of the carrier frequency, ranging code, and navigation message. The nominal frequency of the B3I signal is 1268.520 MHz. The duration of one navigation message bit is 20 milliseconds and the ranging code period is 1 ms. The B3I signal is right-hand circularly polarized and is modulated by binary phase shift keying [8].

B. Range Compression

When the raw data arrive in the RHCP and LHCP antennas, the intermediate frequency (IF) signal collector uses down conversion to record IF signals [19]. Afterward, the IF signals are processed using a software receiver to achieve range compression. To describe this processing clearly, Fig. 2 shows the procedures of signals collection and range compression. The RC data can be written as

$$S_{\text{rc}}(\tau, t) = \Lambda\left[t - \frac{R_\Delta(\tau)}{c}\right]\exp\left[-j2\pi f_d(\tau) t\right] \quad (1)$$

where t is the index of the sampling time in the pulse repetition interval (PRI), τ is the index of PRI period (slow-time), and $\Lambda(\cdot)$ is the amplitude of the cross-correlation function of range codes (triangular function). f_d is the Doppler frequency. R_Δ is a bistatic range, which can be written as

$$R_\Delta(t) = R_{\text{st}}(t) + R_{\text{tr}}(t) - R_{\text{sr}}(t). \quad (2)$$

where R_{st} is the range between the satellite and the target; R_{tr} is the range between the target and the receiver; R_{sr} is the
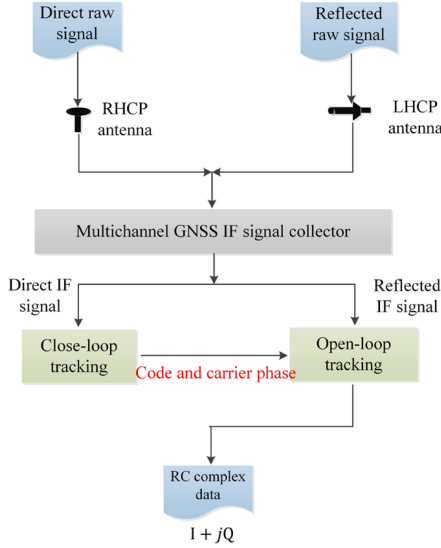
Fig. 2. Flowchart of the multichannel GNSS IF signal collector and range compression in a software-defined receiver.
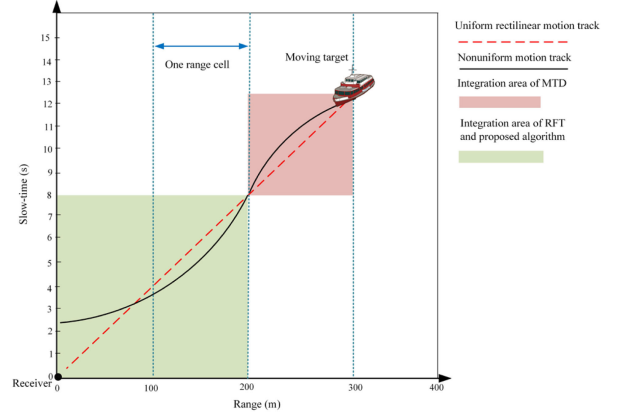

Fig. 3. Different motion tracks and integration areas of three algorithm. The red area and the green area is the integration area of different algorithms. The x-axis is slow-time and the y-axis is range. Assuming 100 m is one range cell.

range between satellite and receiver. $\theta(t)$ is the phase difference between direct signal and reflected signal, which mainly depends on the bistatic range R_Δ. R_Δ is constant if the target is stationary, whereas R_Δ is changeable for maneuvering target. Since the interested target of this article is maneuvering, we will perform a detailed analysis of R_Δ in the following SNR improvement algorithm.

III. EXISTING ALGORITHMS: MTD AND RFT

MTD and RFT are SNR improvement algorithms that are currently used in GNSS-based radar target detection. A brief description is given because we will compare these methods.

Aiming at the target motion state, several researchers have investigated the energy integration algorithms. The algorithms are detailed as follows.

1) MTD algorithm is based on Fourier transform (FT) within one range cell [20]. The traditional algorithm is that $S_{rc}(\tau, t)$ is performed with the FT during the slow-time to accumulate the target's energy coherently. The process is shown as follows:

$$S_{\mathrm{MTD}} = \int_{-T_r/2}^{T_r/2} S_{\mathrm{rc}}(\tau, t) \exp(-j2\pi f_d \tau) \, d\tau \quad (3)$$

where T_r is the dwell time within one range cell; f_d is Doppler frequency, which depends on the radial velocity. Suppose a uniform linear motion, the above coherent integration in one range cell is the MTD method, which is also called Doppler filter bank. The exact Doppler shift can be determined by the maximum output of different filters by searching velocity. Unfortunately, improving the integration gain of MTD further is difficult because of the limited dwell time in a single range cell. It can only integrate energy within one range cell and becomes invalid for solving the RM effect. To illustrate this limitation of MTD in detail, we depicted the integration area of MTD in the red area shown in Fig. 3. Moreover, with regard to

non-uniform motion, the polynomial phase of echo related to the target motion state will make the fast FT based MTD method invalid, that is, the DFM effect is not solved. Therefore, the traditional MTD within slow-time is not the optimal approach for long-time integration to enhance the power of echo. As a result, the traditional algorithm of MTD cannot solve the effects brought by RM and DFM.

2) *RFT Algorithm*: Based on the coupling relationship of velocity, RM, and Doppler frequency of a moving target, RFT is proposed to realize the long-time integration for a target with RM, which may be quite helpful for SNR improvement. The RFT of S_{rc} is defined as [21]

$$S_{\mathrm{RFT}} = \int_{-\infty}^{\infty} S_{rc}\left[\tau, \frac{(R_{\Delta,0} - v_0\tau)}{c}\right] \exp(-j2\pi f_d \tau) \, d\tau \quad (4)$$

where v_0 is initial velocity. From (4), the RFT is essentially a filter bank with different inputs ($R_{\Delta,0}$ and v_0) and outputs. RFT corrects the RM by selecting the data on the trajectory $S_{rc}[\tau, (R_{\Delta,0} - v_0\tau)/c]$ to form a new data vector, then compensates the Doppler offset by the Doppler filter bank $\exp(-j2\pi f_d \tau)$, and finally obtains the condition of long-time integration. Compared with the MTD method in (3), the integration time is not limited by the target velocity and range resolution because the echo is extracted as a vector but related to the motion of target and illuminating time. Therefore, the RFT can solve the RM effect, and more pulses can be integrated coherently within a longer time, which is shown in the green area of Fig. 3. From this green area, the integration gain of RFT can involve multiple range cells that ignore the effect of RM.

However, the effect of DFM caused by the radial acceleration of target still cannot be corrected. Although the Doppler filter function of RFT $exp(-j2\pi f_d \tau)$ is identical to that of MTD, the RFT can solve the RM effect under limited condition (uniformly rectilinear movement). Unfortunately, the effective integration time along the red straight line in Fig. 3 may be limited by the DFM because of accelerated or high-order motion. At the same time, the acceleration will make Doppler and envelope mismatch between the real echoes and the searching parameters

of RFT. Therefore, the integrated peaks in the RFT domain will be broadened, and the coherent integration gain will be inevitably decreased, accordingly.

As a result, we first need to carefully consider the ship motion state and then develop a novel SNR improvement algorithm to compensate the DFM and the RM. Due to the weak power of the navigation signal, the maximum detection range is limited, basically within several kilometers. Under the condition of detection range, the suitable application of GNSS ground-based detection is coastal ports or inland rivers. The ships may have maneuvering operations when docking and leaving the shore due to the low speed of ships in this area. Therefore, building a simple model of uniform motion is not enough. Considering maneuvering target, the bistatic range R_Δ is changeable with time. R_Δ can be written as

$$R_\Delta\ (\tau) = \frac{1}{2}\,a_t\tau^2 + v\tau + R_{\Delta,0} \tag{5}$$

where a_t is radial acceleration, v is radial velocity, and $R_{\Delta,0}$ is the initial bistatic range. In practice, the radial velocity and acceleration are our final purpose of target detection because these two parameters of the noncooperative target are unknown. Because the radial velocity and acceleration correspond to frequency and chirp rate, respectively, the expansion of the Doppler spectrum can be expressed as

$$f_d = \frac{dR_\Delta\ (\tau)}{\lambda d\tau}\ = \frac{d\left(a_t\tau^2\big/2 + v\tau + R_{\Delta,0}\right)}{\lambda d\tau} = f_0\ + \mu\tau \tag{6}$$

where λ is the wavelength of B3I signals (24 cm), f_0 is the central frequency of Doppler, and μ is the chirp rate due to radial acceleration. Based on the above motion model, we propose the FrFT-based SNR improvement algorithm.

IV. FrFT-Based SNR Improvement Algorithm

In this section, we first introduce the principle of FrFT and then give the implementation steps.

A. Proposed SNR Improvement Algorithm Based on FrFT

It can be deduced from (6) that after range compression, the phase of echo is modulated by velocity and acceleration. The Doppler can be approximated as a first-order polynomial, and the chirp rate can be approximated as a quadratic phase term. As a result, we need to compensate the quadratic phase term to improve the outputs of RFT for higher integration gain and use a specific method to achieve the energy integration of FM signal.

Compared with the FT, the FrFT is more suitable for processing nonstationary signals because of its additional degree of freedom, that is, transform angle. The FRFT has included a quadratic form (chirp form) in its kernel function, which makes the linear FM signal integrated as an impulse in the proper FrFT domain [22]. To overcome the problem of the RM and RFM, we derive the RFT idea of extracting echo vector and propose a combinative algorithm to realize long-time integration for the maneuvering of target based on FrFT. Suppose that $f(t,r)$ is a two-dimensional complex function defined in the plane, the
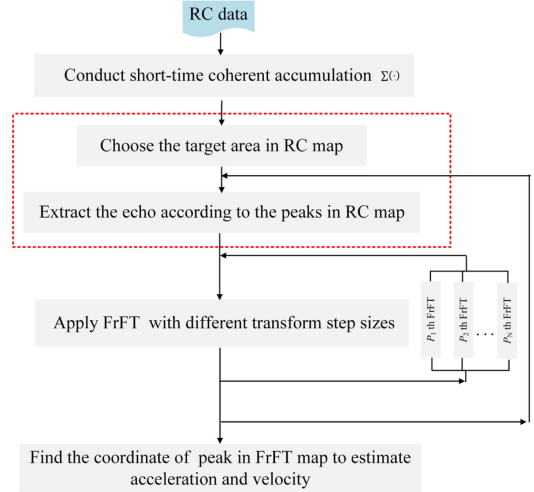

Fig. 4.   Block diagram of the proposed SNR improvement algorithm.

algorithm is defined as

$$G_r\ (\alpha,u) = \mathcal{F}^\alpha\ [f(t,r)] = \int_{-\infty}^{\infty} K_\alpha\,(t,u)\,f(t,r)\,dt \tag{7}$$

where $\mathcal{F}^\alpha$ denotes the operator, $\alpha = \frac{p\pi}{2}$ is the transform angle, p is transform order, u is FrFT domain, and $K_\alpha(t,u)$ is the transform kernel [23]. Specifically, the echo's FrFT can be written as

$$S_{\mathrm{FrFT}} = \int_{-\infty}^{\infty} K_\alpha\,(\tau,u)\,S_{rc}\left[\left(\frac{1}{2}a_t\tau^2 + v\tau + R_{\Delta,0}\right)\Big/c,\tau\right]\,d\tau. \tag{8}$$

The motion parameters v and a_t have explicit physical meanings. We will give the detailed calculation about these two parameters based on the results of FrFT in following section

Equation (8) shows that the FrFT is a linear transform, which is not influenced by the cross-term interference. Fig. 3 shows the diagram of the coherent integration area of the proposed algorithm (green area). The differences and advantages of the algorithm compared with the others are detailed as follows.

It combines the advantages of RFT and FrFT. Thus, it not only has the same function of correcting RM as RFT, but also works well as a useful tool for nonstationary and time-varying signal processing.

The kernel of FrFT is introduced to compensate the DFM due to the high-order motion and to generate the ultimate coherent peak.

It can be regarded as a special Doppler filter bank composed of filters with different transform angles that can compensate and represent the velocity and acceleration simultaneously.

The integration gain will be further improved than the other method (MTD) because it can complete long-time integration.

B. Procedure of the Proposed Algorithm

With regard to clarifying the processing of SNR improvement, Fig. 4 shows the flow chart of the long time (tens of seconds) integration algorithm based on FrFT, which can be divided into four steps. Each processing step will be described as follows.

1) Step 1: Conduct Short-Time Coherent Integration: In GNSS receiver, the signals are sampled from slow time and fast time. The fast sampling frequency corresponds to the sampling frequency f_s of the receiver, while the slow sampling number f_r matches the index of the frame. Therefore, the input RC data can be written as a two-dimensional (2-D) matrix $\mathbf{RC} = S_{rc}(\tau, r)$ for processing, where $r \in [0, f_s]$ is the index of range cell, that is, fast time; $\tau \in [-\frac{T}{2}, \frac{T}{2}]$ is slow time; and T is the dwell time on target.

Under the condition of Beidou GEO satellites, the echo is weak and the RC map is difficult to show the information of target before short-time coherent integration (the raw RC map will be shown in Section V). Therefore, to indicate the trajectory of target in RC map for extracting the target echo, it is important to conduct short-time coherent integration for raw RC data. Notably, the short time is tens of milliseconds, which is shorter than the long time (tens of seconds). By ignoring the amplitude of the cross-correlation function of range codes, the RC data can be written as

$$S_{\mathrm{rc}}(\tau) = \exp\left\{ j\left[2\pi \frac{R_\Delta(\tau)}{\lambda} \right] \right\} + w(\tau) \qquad (9)$$

where $w(\tau)$ is the noise. The signal is directly integrated and written as

$$z = \sum_{\tau=0}^{\mathrm{CIT}-1} \exp\left\{ j\left[2\pi \frac{R_\Delta(\tau)}{\lambda} \right] \right\} + \sum_{\tau=0}^{\mathrm{CIT}-1} w(\tau) \approx \mathrm{CIT}$$

$$\cdot \exp\left\{ j\left[2\pi \frac{R_\Delta(\tau)}{\lambda} \right] \right\} + \sum_{\tau=0}^{\mathrm{CIT}-1} w(\tau) \qquad (10)$$

where CIT is the coherent integration time.

After basic SNR improvement (step 1), the target's echo can be highlighted from the background noise, and thus the RC map can show a bistatic range history of the target that results in showing proper initial parameters.

2) Step 2: Choose the Target Area and Extract Echo in RC Map: In this step, we choose the target area that may include the interest echo. First, based on relative prior information obtained by the experimental scene, such as the approximate width of the river and the range between the river and the receiver, the expected searching scope of bistatic range $[-R_{\Delta,\max}, R_{\Delta,\max}]$ and the range resolution Δr are preset beforehand. The RC data after step 1 in this range scope can be expressed as

$$\mathbf{RC} = \sum_{\boldsymbol{\tau}=(\boldsymbol{n}-1)\times\mathbf{CIT}+1}^{\boldsymbol{n}\times\mathbf{CIT}} S_{rc}(\tau, -r_{\max}+r) \qquad (11)$$

where $n = 12, \ldots, \frac{T}{\mathrm{CIT}}$, $-r_{\max} = \frac{-R_{\Delta,\max}}{\Delta r}$ is the starting range cell; and r is the index of range cell, $r = 12, \ldots, \frac{2R_{\Delta,\max}}{\Delta r}$. Then, the data of correlation peaks in range direction (row direction according to the RC data matrix) are extracted. The extracted data is constructed a new data vector $\mathbf{X}_n$ for next long time integration processing, that is

$$\mathbf{X}_{\boldsymbol{n}} = \max(\mathbf{RC}(:, r))$$

$$= [S_{\mathrm{rc}}(1, r_1)\, S_{\mathrm{rc}}(2, r_2) \cdots S_{\mathrm{rc}}(n, r_n)]^{\mathrm{T}} \qquad (12)$$

where $\max(\cdot)$ is the processing of extracting maximum point of an array, and r is determined by the range direction of peaks.

In [24], the motion model $\frac{1}{2}a_t\tau^2 + v\tau + R_{\Delta,0}$ that represents accelerated or high-order motion is used for searching lines (black curve in Fig. 3) in the RC map (slow time versus range map) to search the target's bistatic range history and to extract the echo according to the history. Unfortunately, the improper searching parameters, such as initial velocity, initial range, and acceleration, may increase computational burden. In this article, we use step 1 to simplify the burden, and the echo can be extracted easily using correlation peaks in the range direction after step 1.

3) Step 3: Apply FrFT: The discrete FrFT with different transform angles can be realized by the decomposition algorithm proposed by Ozaktas [25]

$$\mathcal{F}^\alpha(u) = \frac{\sqrt{\frac{1-j\cdot\cot(\alpha)}{2\pi}}}{2F} \sum_{\tau=-n/2}^{n/2-1} \exp\left(j\pi u^2 \cdot \cot(\alpha) \right)$$

$$\cdot \exp\left(\frac{j\pi\tau^2 \cdot \cot(\alpha)}{4F^2} - \frac{j\pi u\tau \cdot \csc(\alpha)}{F} \right) S_{\mathrm{rc}}\left(\frac{\tau}{2F} \right) \qquad (13)$$

where n is the signal length after step 1, and F denotes the highest frequency component of $S_{\mathrm{rc}}(\tau)$ in slow time.

Two loop iterations are detailed and illustrated as follows.

1) Transform orders for the first iteration are changed. In every iteration, a 1-D searching of p is performed. When inputting a given transform order, the FrFT will output a one-dimension transform results in u domain. Then, changing the transform orders $p_{\mathrm{N}} = p + N\Delta p$ where the number of N depends on the transform step size Δp, and the FrFT will output two-dimension results. The transform step size Δp follows the order from large value to small value (coarse to fine searching). In other words, to simply the computational complexity, the echo is first performed with FrFT using coarse searching to judge the existence of the target. If the FrFT can show a target peak, then the echo is performed with fine searching to improve the integration gain. The specific Δp is determined by the acceleration in such a way that its resolution cannot exceed that target's acceleration.

2) The searching area for the second iteration is changed. Generally, after the FrFT, the echo's energy can be integrated as an intensive peak that represents the target peak. However, if the echo is noise instead of the reflected signals from target, then the FrFT cannot show an intensive peak because the energy of noise cannot be integrated. In this case, we need to select a new searching area for another transform order iteration until the results can show a target peak because the searching area may not involve the target.

By implementing FrFT on the vector $\mathbf{X}_n$ to compensate the DFM and the RM simultaneously, the long-time integration of the maneuvering target's energy is completed.

4) Step 4: Find the Coordinate of Peak and Estimate Parameters: After step 3, the echo of the target has performed long time integration, and the energy has been integrated. Therefore, the FrFT result can form an intensive peak with a relatively

(a)

(b)

Fig. 5. Experimental scene. (a) Schematic diagram of the experimental GNSS-based radar acquisition geometry. (b) Experimental setup of the receiving system.

high SNR. To obtain the optimum result of SNR improvement, the transform step size is set to be finer than before to further accumulate the energy until the SNR of the peak has no increase or slightly increase. If the peak cannot be observed in the FrFT map after changing the transform step size, then the searching area in Step 2 will be chosen again. We will go through all the searching area and note down the corresponding coordinate of peak in the two-dimensional domain (p, u). We can write

$$(p_{\max}, u_{\max}) = \operatorname{argmax}_{p,u} |G_r(p, u)| \qquad (14)$$

where $\operatorname{argmax}(\cdot)$ is the function that output the index of the maximum point, and $G_r(\cdot)$ is the output of FrFT. Since $p = \frac{2\alpha}{\pi}$, we substitute the search of p for the search of α.

We can calculate the motion parameters based on this coordinate because the coordinate $(p_{\max}, u_{\max})$ matches with the motion parameters of the target (acceleration and radial velocity). The calculation is based on the scale factor S. The factor can be written as

$$S = \sqrt{\tau / f_r} \qquad (15)$$

where τ is the number of slow time, and f_r is the sampling number in slow time after step 1 (1000/CIT). The normalized chirp rate $\hat{f}_d$ can be written as

$$\hat{f}_d = -\cot(p\pi/2) \qquad (16)$$

and the truth chirp rate μ can be written as

$$\mu = \hat{f}_d \cdot f_r / S^2 = \hat{f}_d \cdot f_r / \tau. \qquad (17)$$

We can write radial acceleration as

$$a_t = \lambda \cdot \mu. \qquad (18)$$

Besides the acceleration, we can also calculate the velocity of target based on the FrFT domain u. The central frequency f_0 can be written as

$$f_0 = u \cdot \csc(p\pi/2) \qquad (19)$$

and the radial velocity v can be written as

$$v = f_0 \cdot \lambda. \qquad (20)$$

V. FIRST EXPERIMENT RESULTS: CARGO SHIP WITH HIGH RCS

In this section, we conduct a field experiment of moving cargo ship to confirm the SNR improvement of the proposed algorithm. The results of each algorithm step will be illustrated.

A. Experimental Setup

Maneuvering target experiment is conducted using BeiDou C01 and C04 GEO satellites as transmitters of opportunity. Fig. 5 shows the experimental setup of MTD. Fig. 5(a) shows data acquisition geometry during the measurement. The passive receiver is suited at the northeastern bank of the Wuhan Yangtze River Bridge in China. Target of opportunity refers to the commercial ANJI 202 cargo ship, which is more than 700 m away from the receiver and runs in schedule. Fig. 5(b) shows one white RHCP patch antenna for direct signal and one high-gain LHCP helical antenna for reflected signal. The collector is with a sampling frequency of 62 MHz, and the range between samples is approximately 4.8 m. The size of cargo ship is approximately 110 m × 19 m × 15 m (length × width × height).

Here, we give an estimation of RCS. In [26], the RCS of ship depends on the tonnage of interested target. The maximum RCS is approximately

$$\sigma_{\max} = 11.9 \times \log_{10}(\text{tons}) \qquad (21)$$

under the condition of wavelength 0.034 m, where tons is the tonnage of ship. However, in our experiment, the wavelength of B3I signal is 0.24 cm. Thus, the max value $(\sigma_{\max})$ need to plus a conversion coefficient caused by wavelength $10 \times \log_{10}(\lambda^2 / \lambda_{B3}^2) = 10 \times \log_{10}(0.034^2 / 0.24^2) \approx -17\text{dB m}^2$. So, RCS of the cargo ship (approximately 6000 tons) in the article is about $11.9 \times \log_{10}(6000) - 17 \approx 28$ dB m².

Given that GEO satellites are used in this article, the operation of GEO satellites is analyzed in detail. Thus, we can make a reasonable approximation to its azimuth and elevation angles. Here, we take C01 and C04 satellites during the day of the experiment as examples to discuss the variation of satellite elevation. We give the elevation angles calculated by ephemeris
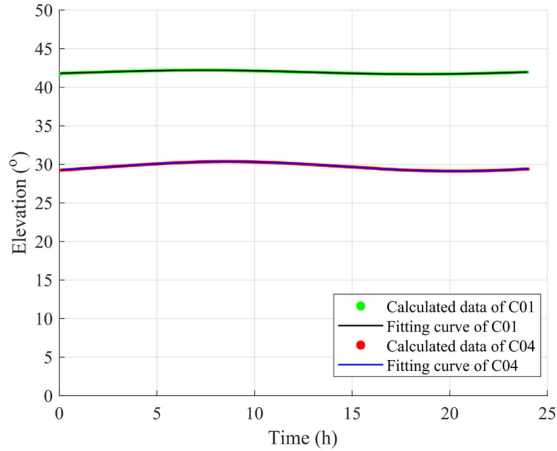
Fig. 6. Elevation angle of two GEO satellites for 24 hours.

TABLE I
ELEVATION ANGLE VARIATION OF TWO SATELLITES OVER DIFFERENT PERIODS

GEO satellite index	Period=2 s	Period=20 s	Period=20 s
C01	≤ 0.13°	≤ 0.13°	≤ 0.13°
C04	≤ 0.44°	≤ 0.44°	≤ 0.44°

for 24 h (see Fig. 6). The black curve shows that the elevation angle of C01 is from 41.71° to 42.22°. The blue curve shows that the elevation angle of C04 is from 30.37° to 29.12°. Based on fitting, we can obtain the periodic relationship between angle and time. The relationship can be written as

$$\text{Ele}_1 = 41.95 - 0.1361\cos(0.2881t) + 0.2162\sin(0.2881t) \tag{22}$$

and

$$\text{Ele}_4 = 29.74 - 0.4431\cos(0.2723t) + 0.4314\sin(0.2723t) \tag{23}$$

where R^2 is 0.9943 and 0.999. RMSE is 0.01323 and 0.01415. According (22) and (23), we can calculate the offset of elevation angle over different time lengths and provide the results given in Table I. This table shows that the offset of the elevation angle during the limited signal acquisition time of 20 s is almost less than 0.5°. Because the periodic offset of the azimuth angles is similar to that of the elevation angles, we ignore the information about the azimuth angles. The offset of azimuth angle can be seen in [27].

B. Short-Time Coherent Integration Results

In the experiment, we collect a time length of 20 s data for analysis. After the range compression, as mentioned in Section II, the raw RC data are stored in a matrix $\mathbf{RC} = S_{\text{rc}}(\tau, r)$, where τ is the index of the PRN period ($\tau = 1, 2, \ldots, 20000$), and r is the index of the range cells. Given the limitation of the river width, only 600 range cells, that is, $r = 1, 2, \ldots, 600$, are considered for processing in each millisecond to reduce the total amount of data.

Here, we conduct a short-time coherent integration, as mentioned in Section IV with CIT = 20 ms depending on the target's velocity. In the time length of 20 ms, we suppose that the target is approximately stationary, and the Doppler frequency is approximately constant. Fig. 7 shows the RC maps (C01 data) of the cargo ship before and after the short-time coherent integration (step 1). In Fig. 7(a), we cannot find the information about the cargo ship in the interested area. However, the nearby stationary targets (far from 80 m) can show an intensive correlation peak history. The reason is that the echo of the cargo ship has a lower SNR than that of the stationary targets. As a result, the echo of the cargo ship is submerged under the noise, and it cannot show a correlation peak history in the RC map. In the other figures, we show part of the bistatic range from 1000 to 1800 m (interested area) as illustration because the stationary targets are out of the scope of this article. Fig. 7(b) shows two areas: area containing target and noise area. From the area that contains target, a bistatic range history of target echo with wide range (two white lines), because of the point spread function of pseudo-random noise code in range compression. As the y-axis of Fig. 7(b) changes from time into frame (the 20 ms data are integrated as one frame), the number of frames in the y-axis becomes 1000 (20 000/20). The two areas in Fig. 7(b) will be used as different searching areas in the following sections. Fig. 8 shows the RC maps of C04 data before and after short-time coherent integration. Similar to C01, Fig. 8(b) shows a bistatic range history with a width after Step 1.

C. SNR Improvement Results

To show the area searching processing and the validity of FrFT-based long-time integration algorithm better, this section is explained in two sections. First, the integration results of the echo from the noise area (no target) are shown. Then, the integration results of the echo from the area containing target are shown.

1) Noise Area: Taking the RC data of C01 [see Fig. 7(b)] as an example, we choose the bistatic range [1500 m, 1800 m] as the noise area according to the order of far to near. After extracting the peak points and FrFT processing, we obtain the FrFT results shown in Fig. 9. The transform order p is determined from 0 to 2, that is, the transform angle $\alpha \in (0, \pi)$. The SNR in FrFT map is the ratio of FrFT result to partial stable area in the map (noise base). Fig. 9(a) shows the result with the step size Δp being 0.2. In this figure, several peaks can be observed. However, no obvious peak is significantly higher than the other peaks, indicating that the energy cannot be integrated by FrFT processing. This situation occurred because of two reasons: First, the searching area does not include the target echo. Second, the step size Δp is not proper for the echo's chirp rate. To solve the second reason, the step size Δp is reset to be finer. The result in energy integration with $\Delta p = 0.02$ is shown in Fig. 9(b). As seen, the peaks are still dispersive because the energy of echo has not been integrated. Based on the above results, we can conclude that this area does not contain target and we need to choose a new searching area.

2) Area Containing Target: The new searching area is rechosen as [1200 m, 1500 m] for new improvement. After extracting
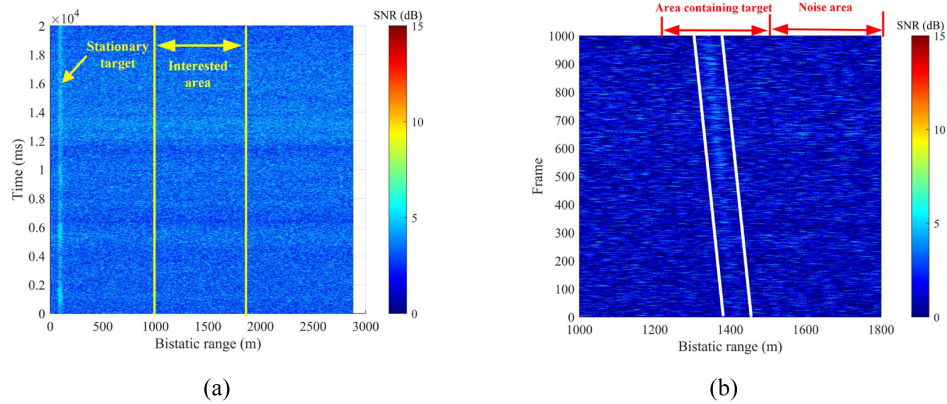
Fig. 7. RC map of signals from C01. (a) Raw RC map before the short-time coherent integration. (b) RC map of signals after the integration. The bistatic range history of target echo is marked by white lines.
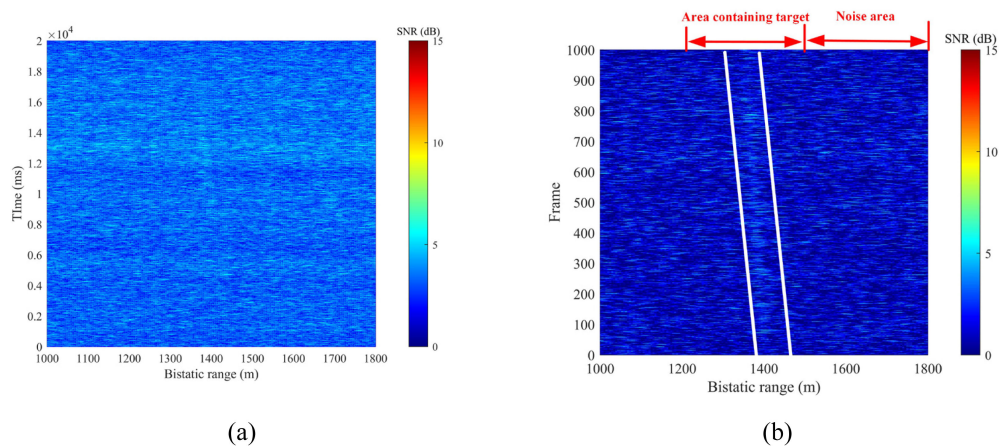

Fig. 8. RC map of signals from C04. (a) Raw RC map before the short-time coherent integration, (b) RC map of signals after the integration. The bistatic range history of target echo is marked by white lines.

the echo and conducting FrFT, the SNR improvement results of C01 echo are shown in Fig. 10. The FrFT result is processed from $p = 0$ to $p = 2$ with $\Delta p = 0.2$ shown in Fig. 10(a). From the figure, we can observe several peaks and one possible target peak with SNR = 14.98 dB with the corresponding coordinate $(p, u) = (1, 14.6)$. Theoretically, $p = 1$ means that the result of FrFT is equal to that of FT, that is, the acceleration of the target is zero. In practice, the interested target is moving with an acceleration. The reason of the difference between the theory and the practice is that the step size Δp is coarse. In this case, obtaining the optimum p is difficult. Therefore, to solve the difference, the step size Δp is chosen to be finer ($\Delta p = 0.02$) for further improvement, as shown in Fig. 10(b). This figure shows a more obvious peak than Fig. 10(a), with the SNR being increased by 1.74 dB. The coordinate of this peak is $(p, u) = (0.98, 14.85)$. To be close to the real target peak, we choose $\Delta p = 0.002$ [see Fig. 10(c)] to observe the SNR of echo peak. The SNR of the peak in Fig. 10(c) is 18.08 dB, and the corresponding coordinate is $(p, u) = (0.984, 14.85)$. When the step size is further chosen to be finer, that is, $\Delta p = 0.0002$, the SNR is increased slightly. To guarantee the effective SNR improvement and simplify the

TABLE II
SNRs AND THE PEAK'S COORDINATES OF C01 DATA

Step size	$\Delta p = 0.2$	$\Delta p = 0.02$	$\Delta p = 0.002$
SNR (dB)	14.98	16.72	18.08
p of target peak	1	0.98	0.984
u of target peak	14.6	14.85	14.85

computational complexity, we chose the step size $\Delta p = 0.002$ as the optimum step size. Fig. 10(d) shows the vertical view of Fig. 10(c). Fig. 10(d) indicates that the target peak is formed by several bright lines converging at one coordinate. In this case, the target peak integrates the gain of the lines. From the definition of FrFT, when one transform order p is input, FrFT outputs one corresponding u domain. The energy of the echo is distributed in u domain if this p is not suitable for the chirp rate of the echo. When several input values are available, the bright lines are formed among multiple u domains. To show the values of coordinates and peaks clearly, the values are given in Table II.

To compare with the SNR improvement performance of MTD and RFT methods, we also use the MTD and RFT to integrate
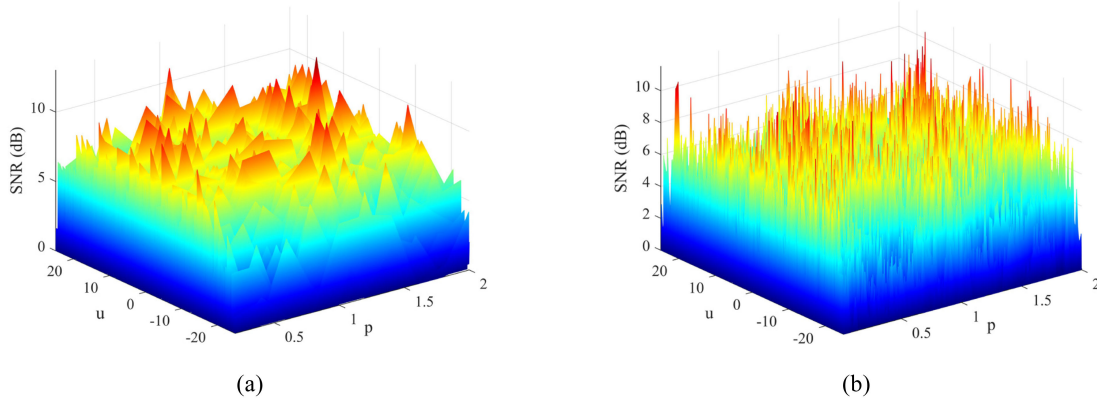
Fig. 9. FrFT map in (p, u) domain with $p \in (02)$. (a) FrFT map of signals from C01 with the step size of p is 0.2. (b) FrFT map of signals from C01 with the step size of p is 0.02.
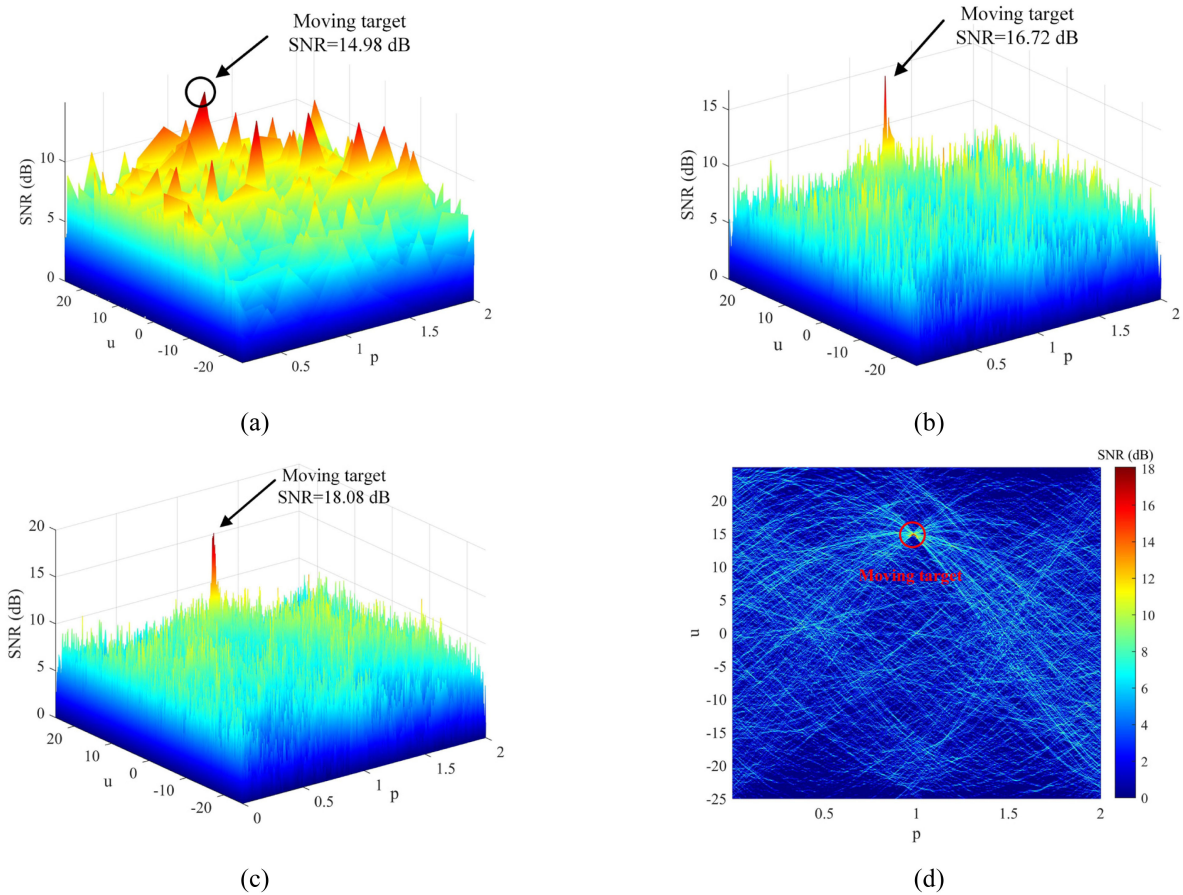

Fig. 10. FrFT map in (p, u) domain with $p \in (02)$. (a) FrFT map of signals from C01 with $\Delta p = 0.2$. (b) FrFT map of signals from C01 with $\Delta p = 0.02$. (c) FrFT map of signals from C01 with $\Delta p = 0.002$. (d) p-u plane graph of the $\Delta p = 0.002$.

the echo's energy and show the results in Fig. 11. Owing to the approximately stable motion state of GEO satellites (the elevation angle variation is less than $0.13°$ during 20 s), we can ignore the Doppler frequency brought by satellite. The C01 RC data in Fig. 7(b) are selected to be enhanced with MTD and RFT methods. Since the target's echo includes RM within a long time, we first utilize the partial data from 0 to 2000 ms to

guarantee the echo within one range cell of 293. Then, we utilize the whole 20000 ms data. Fig. 11(a) shows the integration gain using the traditional MTD method. The red line (the first 2000 ms) illustrates that the energy is integrated as an obvious peak at the range cell (bistatic range 1417 m and SNR = 13.47 dB) while the blue line (the whole 20000 ms) cannot show an obvious peak around the range cell of 293. The reason is that the effect
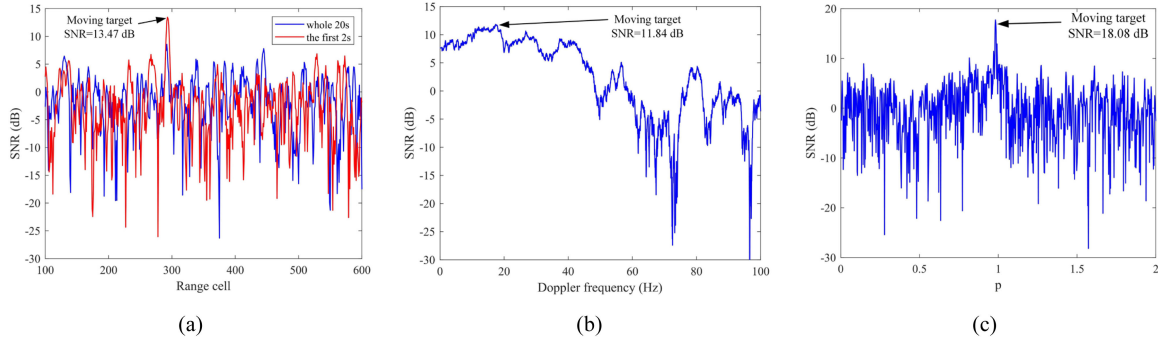
Fig. 11.   SNR improvement of C01 by MTD and RFT methods, respectively. (a) Results of MTD (the red line is the result of the first 2 s RC data, and the blue line is the result of the 20 s RC data). (b) Result of RFT (20 s RC data). (c) Cross-section of FrFT with $u = 14.85$.

of RM can be ignored within the short time of 2000 ms, and the echo can obtain an effective SNR improvement. When the time length is extended to 20 000 ms, the effect of RM cannot be solved. In this case, the integration gain is poorer compared with the former.

The results of RFT method are shown in Fig. 11(b). We utilize the whole 20 000 ms data for RFT method. The target peak has a SNR of 11.84 dB, and the corresponding Doppler frequency (x-axis) is 17.34 Hz. Compared with the result of the red line in Fig. 11(a), the SNR is deceased by 1.63 dB. The reasons of this decrease are as follows.

1) The integration time of RFT (20 000 ms) is longer than that of MTD (2000 ms). In this case, the velocity variation is slightly during short time and thus the identical f_d of the Doppler filter function $H_v(\tau) = \exp(-j2\pi f_d \tau)$ is more suitable for MTD rather than RFT.

2) As the echo includes range curvature due to the DFM, the data vector of RFT $S_{rc}[\tau, (R_{\Delta,0} - v_0\tau)/c]$ includes a lot of noise instead of the interested echo.

To compare with the MTD and RFT, we show the cross section ($u = 14.85$) of FrFT result [see Fig. 10(c)] in Fig. 11(c). Comparing with the results in Fig. 11(a) and (b), the SNR of target peak in Fig. 11(c) is improved by 4.61 and 6.24 dB based on the proposed FrFT-based algorithm, respectively.

Here, we conduct the same improvement processing to C04 RC data [see Fig. 8(b)] and obtain the results shown in Fig. 12. First, in Fig. 12(a) with $\Delta p = 0.2$, the SNR of the possible target peak is 15.37 dB and the corresponding coordinate is $(p, u) = (1, 9.5)$. Then, in Fig. 12(b) with $\Delta p = 0.02$, the SNR is 17.71 dB of the peak increasing by 2.34 dB, and the peak's coordinate is $(p, u) = (0.98, 9.35)$. Finally, in Fig. 12(c) with $\Delta p = 0.002$, the SNR of the peak is 17.32 dB and the corresponding coordinate is the same as the coordinate in Fig. 12(b). Fig. 12(d) is the vertical view of Fig. 12(c). Similar to Fig. 10(d), Fig. 12(d) shows the target peak formed by several bright lines. Table III gives the SNR improvement results of C04's echo clearly (the SNRs and coordinates of the peaks).

Fig. 13 shows the SNR improvement results of MTD and RFT methods. Fig. 13(a) shows the result of MTD method with two time lengths of 2000 and 20 000 ms (the elevation angle variation is less than $0.44°$). The red line illustrates that the energy is integrated at the range cell of 291 (bistatic range 1408 m), and

TABLE III
SNRs AND THE PEAK'S COORDINATES OF C04 DATA

Step size	$\Delta p=0.2$	$\Delta p=0.02$	$\Delta p=0.002$
SNR (dB)	15.37	17.71	17.32
p of target peak	1	0.98	0.984
u of target peak	9.5	9.35	9.35

the SNR of the target peak is 15.25 dB. The blue line cannot show obvious peaks. The results of RFT method are shown in Fig. 13(b). The SNR of the target peak is 13.41 dB, and the corresponding Doppler frequency (x-axis) is 10.44 Hz. Comparing with the MTD and RFT, the cross section of FrFT result with $u = 9.35$ [see Fig. 13(c)] shows that the proposed algorithm can improve the SNR by 2.07 and 3.91 dB, respectively.

Based on the SNR improvement results via MTD, RFT and FrFT-based algorithm, two points may be concluded as follows.

1) Since the SNR improvement performance of MTD is subject to RM and DFM, the processing data of MTD are limited by one range cell. Although the RFT makes use of longer time length for integration, it is still influenced by DFM.

2) The proposed FrFT-based SNR improvement algorithm can correct the RM and DFM. Comparing with the MTD and the RFT, the SNR of C01 echo is approximately increased by 4.61 and 6.24 dB, and the SNR of C04 echo is approximately increased by 2.07 dB and 3.91 dB, respectively.

D. Estimation of Radial Acceleration and Radial Velocity Based on FrFT Results

We can calculate the parameters based on step 4 (see Section V-D) because the coordinate of the target peak (p, u) is determined by the motion parameters of the target (radial acceleration and radial velocity). The observation time is 20 000 ms, and the optimum p of target peak for C01 and C04 are 0.984 and 0.98, respectively.

To verify the accuracy of the calculated parameters based on FrFT results, we give the acceleration calculated by range-Doppler (RD) processing [19]. Fig. 14 shows the chirp rates of two satellites' data based on RD processing. From the figures, the Doppler frequency shows a linear variation over time.
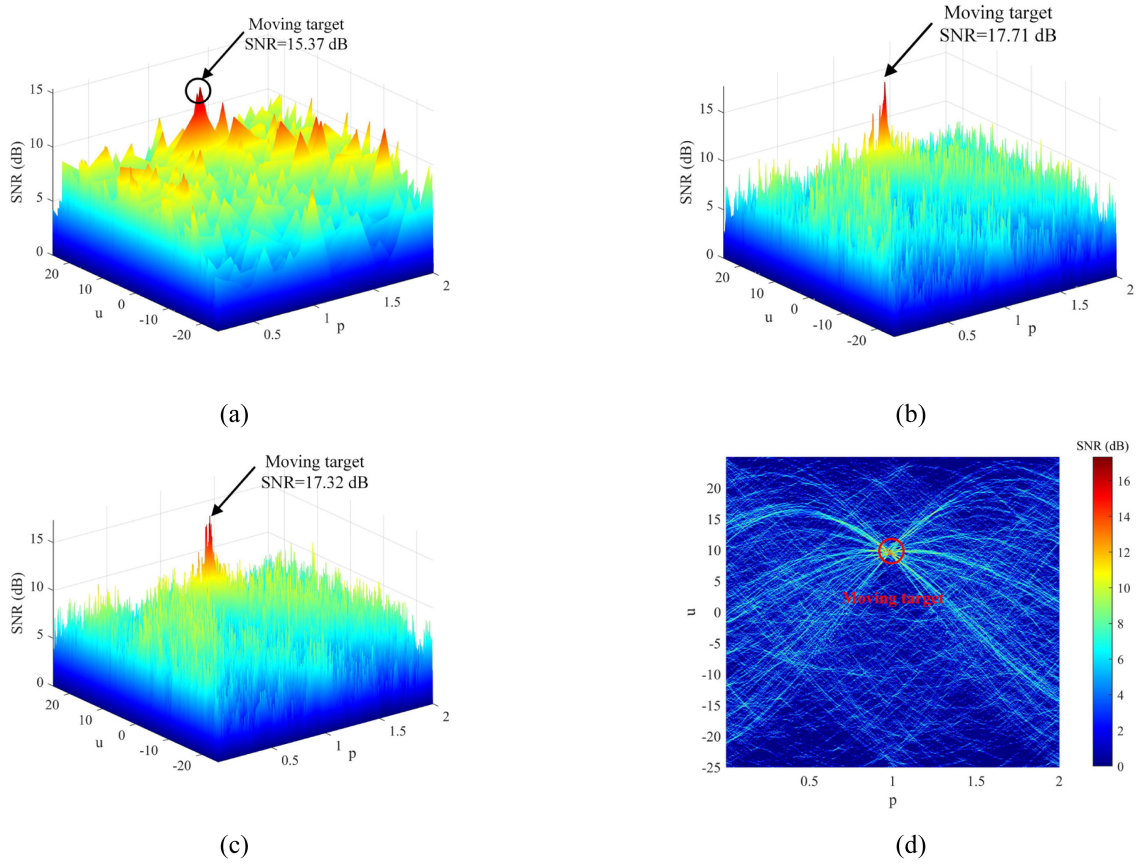
Fig. 12. FrFT map in (p, u) domain with $p \in (02)$. (a) FrFT map of signals from C04 with $\Delta p = 0.2$. (b) FrFT map of signals from C04 with $\Delta p = 0.02$. (c) FrFT map of signals from C04 with $\Delta p = 0.002$. (d) $p - u$ plane graph of the $\Delta p = 0.002$.
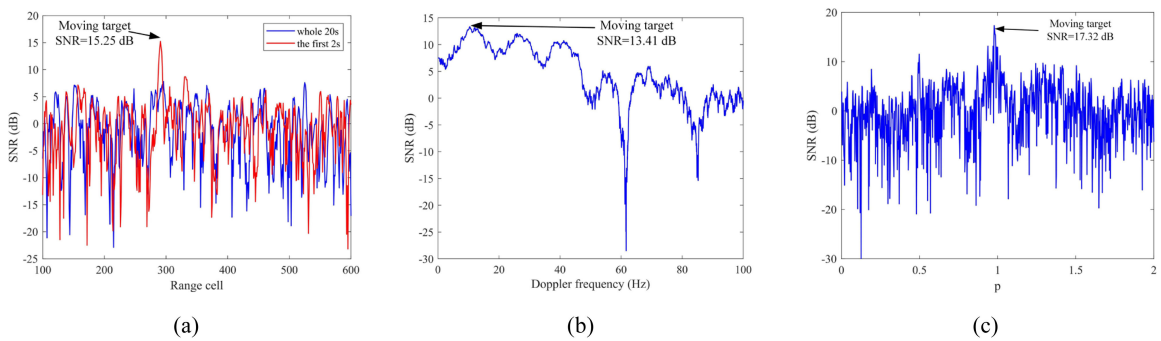

Fig. 13. SNR improvement of C04 by MTD and RFT methods, respectively. (a) Results of MTD (the red line is result of the first 2 s RC data, and the blue line is result of the 20 s RC data). (b) Result of RFT (20 s RC data). (c) Cross section of FrFT with $u = 9.35$.

Table IV gives the calculated parameters based on FrFT and RD processing, including radial acceleration a_t and radial velocity v. The calculated parameters of FrFT results are close to the results of RD processing. Although the calculated accelerations based on FrFT results have deviations that may be resulted from the noise in the step of extracting data, we can use the proposed algorithm to estimate the motion parameters of the target.

Moreover, the target speed recorded by automatic identification system (https://ais.msa.gov.cn) is nine knots (4.63 m/s).

TABLE IV
CALCULATED MOTION PARAMETERS BASED ON FRFT AND RD PROCESSING

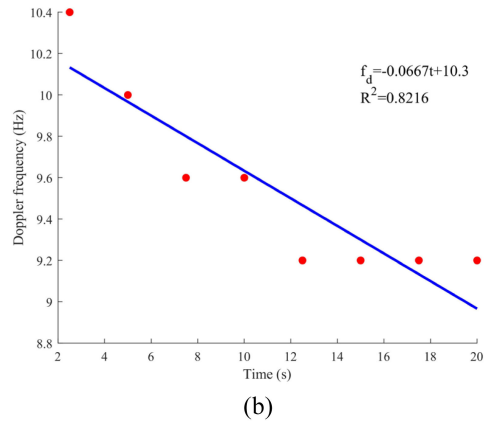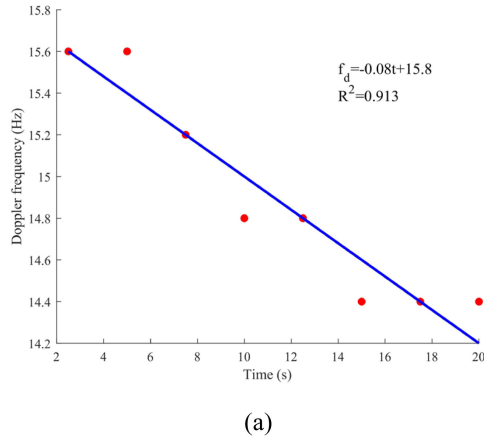| GEO satellites	C01	C04
a_t based on FrFT (m/s^2)	0.015	0.0188
a_t based on RD processing (m/s^2)	0.0192	0.016
v based on FrFT (m/s)	3.567	2.245
v based on RD processing (m/s)	3.792	2.472

Fig. 14. Chirp rate during the time from 0 s to 20 s. (a) Chirp rate of reflected signals of C01. (b) Chirp rate of reflected signals of C04.
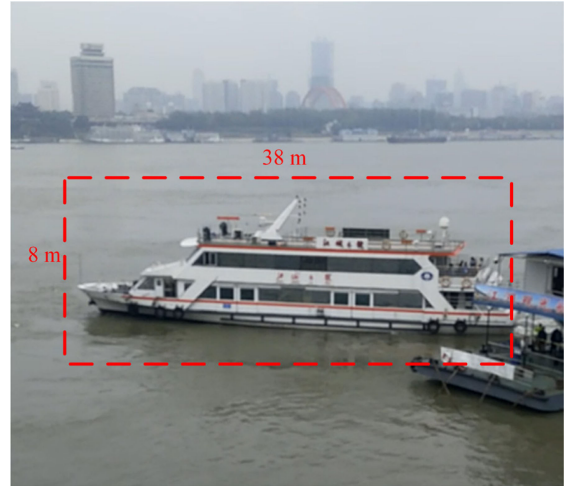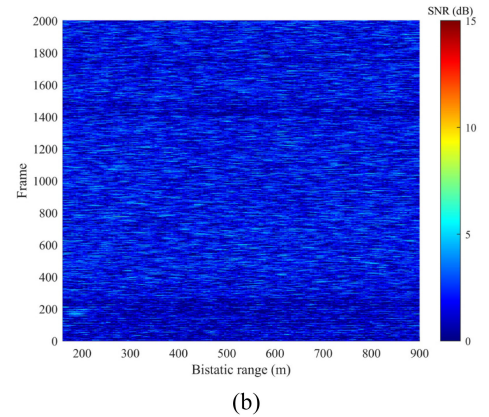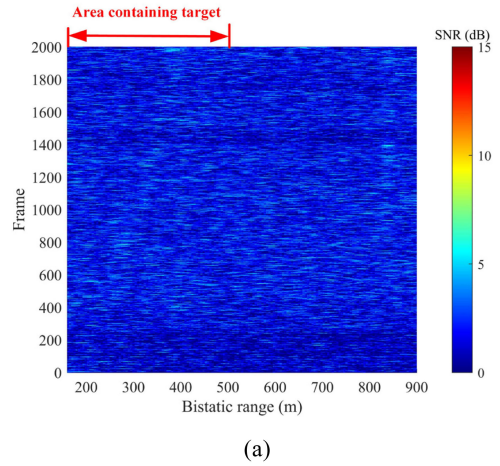

Fig. 15. Photograph of the moving ferry.

Fig. 16. RC map after shot time coherent integration. (a) RC map of signals from C04. (b) RC map of signals from C01.

The estimated motion parameters based on FrFT conforms to the geometry projection relationship.

VI. SECOND EXPERIMENT RESULTS: FERRY WITH LOW RCS

To explore the validity of the FrFT algorithm for target with low RCS, we use the reflected signals of a ferry to conduct the SNR improvement. Fig. 15 shows the photograph of the ferry. The size of the ferry is approximately 38 m $\times$ 8 m $\times$ 8 m with an estimated RCS $\approx$ 15 dB m^2. In the data acquisition, the ferry runs away from the antennas (from southwest to northeast). Compared with the cargo ship, the ferry has two different characteristics.

The RCS of the ferry is less than that of the cargo ship.

The velocity of the ferry is faster than that of the cargo ship.

These two characteristics result in the lower intensive echo, thereby bringing difficulty to target detection based on GNSS bistatic radar system.

In the experiment of the ferry, the 40 s data are collected. After the data are processed with range compression, we conduct a short-time coherent integration with CIT = 20 ms. Fig. 16 shows the RC maps of reflected signals from C04 and C01 satellites. With regard to C04 RC data, Fig. 16(a) can show a bistatic range history of the ferry, although the history has low SNRs

sometimes. Fig. 16(b) shows that the C01 data are even worse compared with C04, and thus the history cannot be observed.

In this section, the FrFT results will be illustrated by two subsections: the SNR improvement results of C04 RC data and C01 RC data.
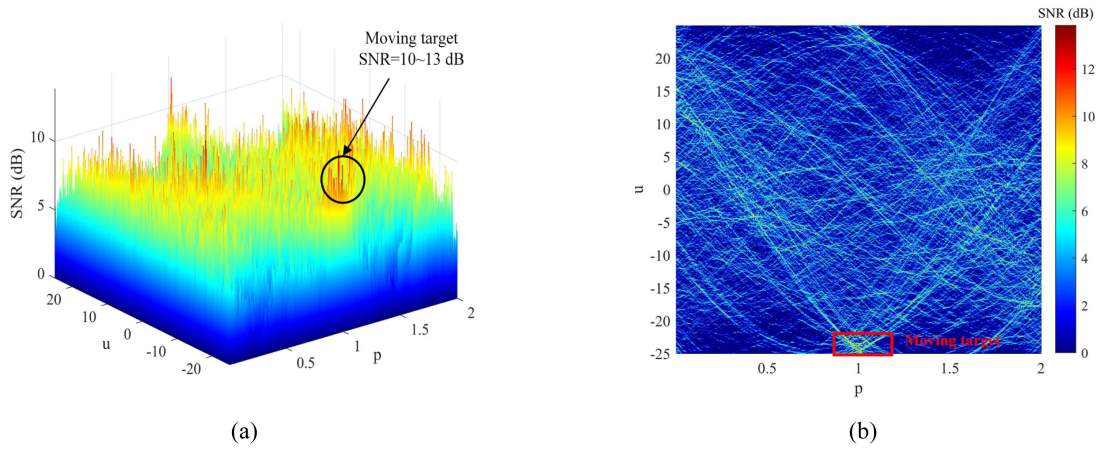
(a)

(b)

Fig. 17.   FrFT map of the first 20 s C04 data. (a) FrFT map with $\Delta p = 0.002$. (b) $p-u$ plane graph of the $\Delta p = 0.002$.
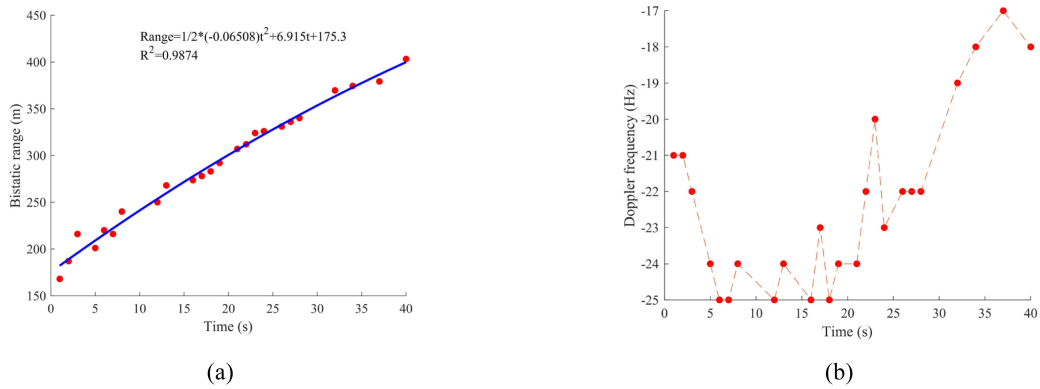

(a)

(b)

Fig. 18.   Bistatic range and Doppler frequency during the time from 0 s to 40 s (C04 satellites). (a) Bistatic range. (b) Doppler frequency.
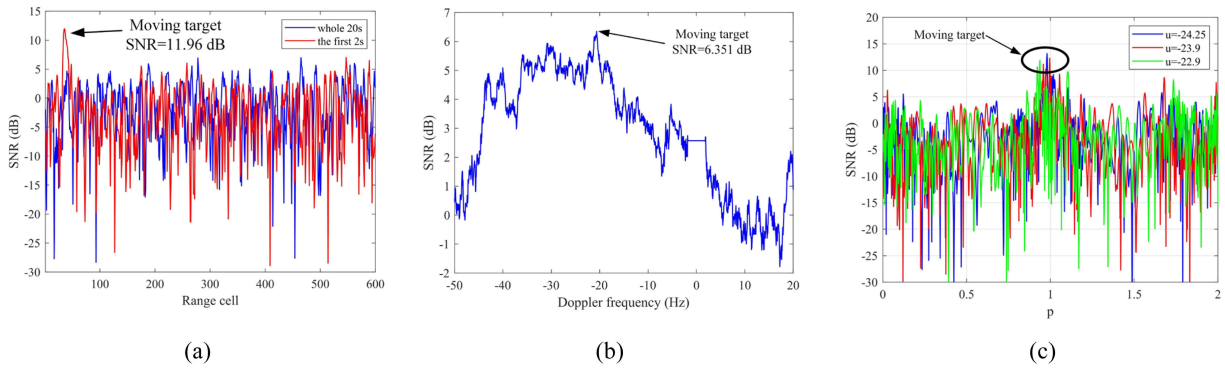

(a)

(b)

(c)

Fig. 19.   SNR improvement of C04 by MTD and RFT methods, respectively. (a) Results of MTD (the red line is the time length of 2 s data, and he blue line is 20 s data. (b) Result of RFT for 20 s data. (c) Cross section of FrFT with different u.

A. SNR Improvement Results of C04 Data

From Fig. 16(a), the intensity of the first 20 s data are higher than that in the second 20 s. Consequently, we first divide the C04's RC data [see Fig. 16(a)] into two parts: the first 20 s data and the whole 40 s data. Then, we conduct the improvement

algorithm for these two parts. The elevation angle variation during 40 s is less than $0.44°$. Therefore, in the SNR improvement processing, the offset of elevation angle can be ignored.

1) SNR Improvement Results of the First 20 s Data: Fig. 17 shows the FrFT maps of C04 RC data in Fig. 16(a) with $\Delta p = 0.002$. Fig. 17(a) shows that the target peaks marked
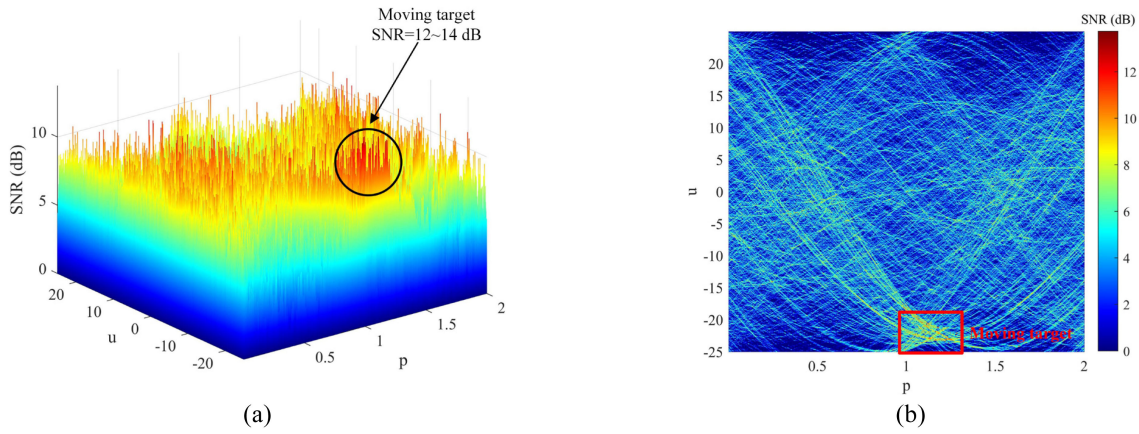
Fig. 20. FrFT map of the 40 s C04 data . (a) FrFT map with $\Delta p = 0.002$. (b) $p - u$ plane graph of the $\Delta p = 0.002$.
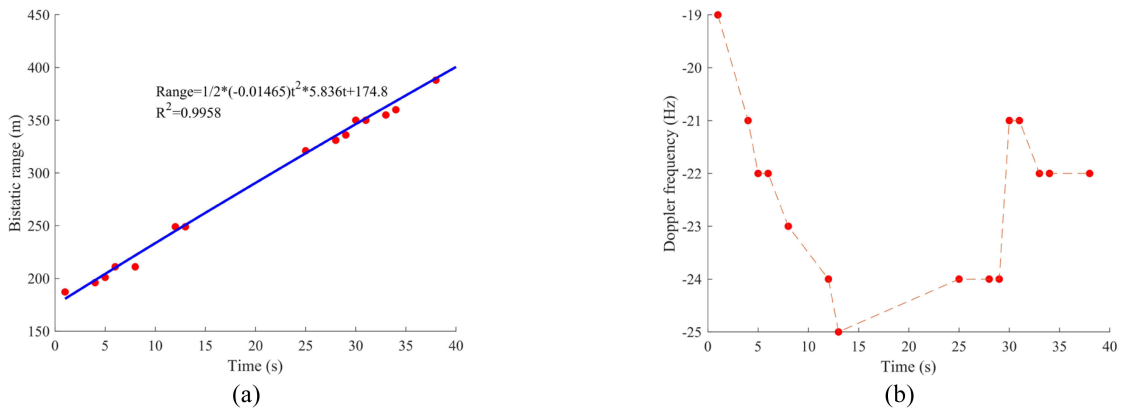

Fig. 21. Bistatic range and Doppler frequency during the time from 0 s to 40 s (C01 satellites). (a) Bistatic range. (b) Doppler frequency.
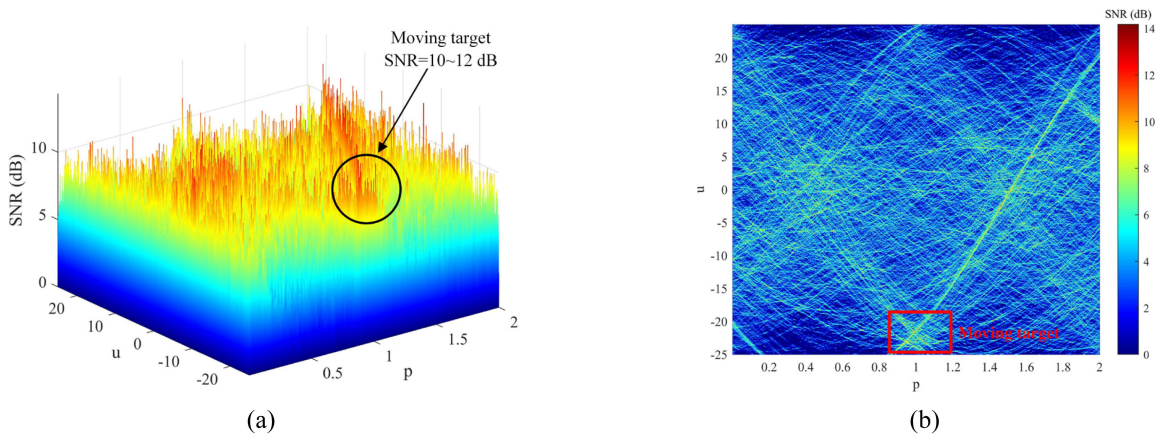

Fig. 22. FrFT map of the 40 s C01 data. (a) FrFT map with $\Delta p = 0.002$. (b) $p - u$ plane graph of the $\Delta p = 0.002$.

with the black circle have an approximate SNR scope from 10 dB to 13 dB. Moreover, the corresponding vertical view [see Fig. 17(b)] illustrates that the energy of echo marked with red rectangle is integrated around $p \in [0.84, 1.012]$. Rather than the intensive peak in cargo ship experiment, the target peaks of the ferry are slightly dispersive.

To analyze the reason for the dispersive peaks, we calculate the RD maps of the target. By recording the bistatic range and Doppler frequency information, we discuss the impact brought by target motion state. Here, we select the time length of 1 s to generate RC submaps that are converted into RD data. To clearly describe the results of RD processing, here, we take the whole

TABLE V
MOTION PARAMETERS BASED ON FrFT AND RD PROCESSING

Processing	FrFT	RD
a_t (m/s²)	[-0.111, 0.011]	[-0.137, 0.016]
v (m/s)	[-5.28, -5.76]	-5.669

40 s raw RC data to conduct the RD processing. In this case, the repeated description of RD data in the following subsection can be avoided. Due to the weak energy of echo in the last 15 s data, we can only obtain 25 RD maps (1 s RC data are transformed into one RD map) for recording the bistatic range, as well as the Doppler frequency. The information of bistatic ranges and the Doppler frequencies is shown in Fig. 18. Fig. 18(a) shows that the bistatic range is gradually increasing, and it can satisfy the high-order motion relationship well ($R^2 = 0.9874$). The Doppler frequency shown in Fig. 18(b) has a considerable variation. From 0 to 7 s, the chirp rate is negative and the Doppler frequency is from -21 to -25 Hz. From 8 to 20 s, the chirp rate is approximately zero with slight fluctuations, and the Doppler frequency is about -24.5 Hz. From 21 to 40 s, the chirp rate is positive, and the Doppler frequency is from -24 to -17 Hz. Therefore, the variation of Doppler frequency in the first 20 s causes the dispersive peaks in Fig. 17 because the chirp rate directly influences the transform order p of FrFT. Based on the coordinate of target peaks in Fig. 17, we can obtain the motion parameters within a certain range given in Table V.

Here, we also conduct the MTD and RFT method to compare with the FrFT-based algorithm. Fig. 19(a) shows the SNR improvement results of MTD. The red line shows an obvious target peak (SNR = 11.96 dB) at the range cell of 36, while the blue line cannot show obvious peaks. Fig. 19(b) shows the SNR improvement result of RFT. The SNR of the target peak is 6.35 dB, and the corresponding Doppler frequency (x-axis) is -20.63 Hz. Fig. 19(c) gives the cross-sections of FrFT results with $u = -22.9, -23.9$, and -24.25. When u decreases, transform orders p that correspond to the peaks have a tendency towards 1 because of the variation of Doppler frequency from 0 s to 20 s (the chirp rate is approximately from negative to zero) in Fig. 18(b). Moreover, the SNR of the peaks is about 13.17 dB, and it increased by 1.21 and 6.82 dB compared with MTD and RFT, respectively.

2) SNR Improvement Results of the 40 s Data: In the following section, the first 20 s data are analyzed. Here, we take the whole 40 s data for FrFT processing to further investigate the proposed algorithm. Fig. 20 shows the improvement results using the 40 s C04 RC data. Fig. 20(a) shows that the target peaks marked with black circle are more dispersive than the peaks in Fig. 17(a). The SNRs of these peaks are approximately 12 to 14 dB. Fig. 20(b) shows that the transform orders p are almost greater than 1 ($p \in [1.1, 1.2]$). Explaining the dispersive peaks and the variation of p is not difficult when the variation of Doppler frequency in Fig. 18(b) is considered. Comparing the first 20 s, the Doppler frequency has a considerable variation during the whole 40 s, and the chirp rate is positive most of time (50% of 40 s). Since the 40 s data are worse than the first 20 s

data in terms of SNR and motion state, the SNR improvement results of MTD and RFT are not calculated.

B. SNR Improvement Results of C01 Data

Although the RC map of C01 processed with short-time coherent integration [see Fig. 16(b)] cannot show the bistatic range history of the target, the target information (bistatic range and Doppler frequency) can be observed from 15 RD maps. The remainder of the RD maps (25 maps) cannot show the information because of the low SNR of echo. Fig. 21(a) shows the relationship between bistatic range and time based on RD processing. This figure shows that the bistatic range satisfies the high order motion relationship with $R^2 = 0.9958$. Fig. 21(b) shows the variation Doppler frequency over time. The trend of the Doppler frequency is similar to the trend in Fig. 18(b). Considering that we cannot use the range information of the ferry in Fig. 16(b) to choose the target area, we use the bistatic range calculated by RD processing as the target area for extracting the echo. Fig. 22 shows the FrFT results of 40 s C01 RC data with $\Delta p = 0.002$. Fig. 22(a) shows that the target peaks marked with black circle are dispersive, and the corresponding SNRs are low (approximately from 10 to 12 dB). The reason for this result is the variation of the Doppler frequency in Fig. 21(b). Moreover, the low SNR of C01 RC data itself has an impact on the final FrFT results.

Based on the FrFT algorithm for enhancing SNR of C01 and C04 GNSS signals, two conclusions about the raw data and the interest target can be obtained in this section. First, FrFT algorithm improves the SNR of echo from maneuvering target effectively. For example, the improvement contrast between the first 20 s data of C04 and the whole 40 s data of C04. Second, the drastic variation of the target acceleration affects the SNR improvement of the FrFT-based algorithm.

VII. CONCLUSION

In this article, we have investigated the potential of using GEO satellites as space-based illuminators of opportunity for inland river monitoring application. Particularly, the focus has been on the algorithm that can properly integrate the echoes from the maneuvering target over a long observation time to counteract the low power budget of the transmitted signal that reaches the ground surface.

Aiming at this purpose, we first analyze the reflected signal model of maneuvering target. The quadratic term of echo may lead to the DFM and RM during the long observation time because of the accelerated motion, thereby reducing the integration gain. Then, we utilized jointly short-time coherent integration and long-time integration to solve the effect of RM and DFM for improving the power of echo. Furthermore, we conduct two field experiments to validate the effectiveness of the proposed algorithm. In the cargo ship experiment, compared with MTD and RFT algorithms, the proposed algorithm can increase the SNR by approximately 3 and 5 dB, respectively. In the ferry experiment, compared with MTD and RFT algorithms, the proposed algorithm can increase the SNR by approximately 1.21 and 6.82 dB, respectively. Also, according to the target

peak's coordinate of the FrFT map, we can obtain a by-product of motion parameters. From the two experimental results, the focused energy in the first experiment is high due to the high RCS and stable acceleration of cargo ship. The focused energy of the second experiment is relatively low because of the low RCS and time-vary acceleration of ferry. As a result, the proposed algorithm is more suitable for the target with a stable acceleration rather than a time-varying acceleration.

Remarkably, the proposed SNR improvement algorithm can show an effective integration gain aiming at the target with stable motion (mainly stable acceleration). Aiming at real engineering applications, the future work will explore the potential of an improvement algorithm for multiple maneuvering targets while being in the same interested area. Moreover, the improvement limitation brought by the variation of acceleration need to be solved.

REFERENCES

[1] G. Mazurek, K. Kulpa, M. Malanowski, and A. Droszcz, "Experimental seaborne passive radar," *Sensors,* vol. 21, 2021, Art. no. 2171.

[2] M. Płotka, K. Abratkiewicz, M. Malanowski, P. Samczynski, and K. Kulpa, "The use of the reassignment technique in the time-frequency analysis applied in VHF-based passive forward scattering radar," *Sensors,* vol. 20, 2020, Art. no. 3434.

[3] J. Shen, J. Yi, X. Wan, D. Xie, and F. Cheng, "Robust DOA estimation for passive radar with target signals mixed in the reference channel," *IEEE Geosci. Remote Sens. Lett.*, vol. 18, no. 3, pp. 456–460, Mar. 2021.

[4] N. Ustalli, D. Pastina, and P. Lombardo, "Target motion parameters estimation in forward scatter radar," *IEEE Trans. Aerosp. Electron. Syst.,* vol. 56, no. 1, pp. 226–248, Feb. 2020.

[5] K. Chetty, Q. Chen, and K. Woodbridge, "Train monitoring using GSM-R based passive radar," in *Proc. IEEE Radar Conf.*, 2016, pp. 1–4.

[6] Z. He, Y. Yang, and W. Chen, "A hybrid integration method for moving target detection with GNSS-based passive radar," in *IEEE J. Sel. Topics Appl. Earth Observ. Remote Sens.,* vol. 14, pp. 1184–1193, Nov. 2020.

[7] H. Zeng, J. Chen, P. Wang, W. Liu, X. Zhou, and W. Yang, "Moving target detection in multi-static GNSS-Based passive radar based on multi-Bernoulli filter," *Remote Sens.,* vol. 12, 2020, Art. no. 3495.

[8] C. S. N. Office, "BeiDou navigation satellite system signal in space interface control document open service signal B3I (Version 1.0)," 2018.

[9] Z. Xu, C. J. Baker, and S. Pooni, "Range and Doppler cell migration in wideband automotive radar," *IEEE Trans. Veh. Technol.,* vol. 68, no. 6, pp. 5527–5536, Jun. 2019.

[10] X. Rao, H. Tao, J. Su, X. Guo, and J. Zhang, "Axis rotation MTD algorithm for weak target detection," *Digit. Signal Process.*, vol. 26, pp. 81–86, 2014.

[11] P. Huang, G. Liao, Z. Yang, X. Xia, J. Ma, and J. Ma, "Long-time coherent integration for weak maneuvering target detection and high-order motion parameter estimation based on keystone transform," *IEEE Trans. Signal Process.,* vol. 64, no. 15, pp. 4013–4026, Aug. 2016.

[12] J. Yu, J. Xu, Y. Peng, and X. Xia, "Radon-Fourier transform for radar target detection (III): Optimality and fast implementations," *IEEE Trans. Aerosp. Electron. Syst.,* vol. 48, no. 2, pp. 991–1004, Apr. 2012.

[13] J. Xu *et al.*, "Adaptive radon–Fourier transform for weak radar target detection," *IEEE Trans. Aerosp. Electron. Syst.,* vol. 54, no. 4, pp. 1641–1663, Apr. 2018.

[14] Y. Song, T. Jin, Y. Song, and Y. Zhang, "An improved radon-Fourier transform coherent integration method," *IEEE Access,* vol. 7, pp. 138593–138602, 2019.

[15] D. Pastina *et al.*, "Maritime moving target long time integration for GNSS-based passive bistatic radar," *IEEE Trans. Aerosp. Electron. Syst.,* vol. 54, no. 6, pp. 3060–3083, Dec. 2018.

[16] H. Ma *et al.*, "Maritime moving target indication using passive GNSS-based bistatic radar," *IEEE Trans. Aerosp. Electron. Syst.,* vol. 54, no. 1, pp. 115–130, Feb. 2018.

[17] D. Pastina, F. Santi, F. Pieralice, M. Antoniou, and M. Cherniakov, "Passive radar imaging of ship targets with GNSS signals of opportunity," *IEEE Trans. Geosci. Remote Sens.,* vol. 59, no. 3, pp. 2627–2642, Mar. 2021.

[18] Z. Li, F. Santi, D. Pastina, and P. Lombardo, "A multi-frame fractional fourier transform technique for moving target detection with space-based passive radar," *IET Radar, Sonar Navig.,* vol. 11, pp. 822–828, 2016.

[19] Y. Li, S. Yan, J. Gong, and F. Zeng, "SNR enhancement of back scattering signals for bistatic radar based on beidou GEO satellites," *Remote Sens.,* vol. 13, no. 7, 2021, Art. no. 1254.

[20] X. Zhou, P. Wang, J. Chen, H. Zeng, and Z. Pei, "Experimental results for GNSS-R based moving target indication," in *Proc. IEEE Int. Geosci. Remote Sens. Symp.*, 2020, pp. 2819–2822.

[21] J. Xu, J. Yu, Y. Peng, and X. Xia, "Radon-Fourier transform for radar target detection, Part I: Generalized Doppler filter bank," *IEEE Trans. Aerosp. Electron. Syst.,* vol. 47, no. 2, pp. 1186–1202, Apr. 2011.

[22] S. Pei and J. Ding, "Fractional Fourier transform, wigner distribution, and filter design for stationary and nonstationary random processes," *IEEE Trans. Signal Process.,* vol. 58, no. 8, pp. 4079–4092, Aug. 2010.

[23] L. B. Almeida, "The fractional Fourier transform and time-frequency representations," *IEEE Trans. Signal Process.,* vol. 42, no. 11, pp. 3084–3091, Nov. 1994.

[24] X. Chen, J. Guan, N. Liu, and Y. He, "Maneuvering target detection via radon-fractional Fourier transform-based long-time coherent integration," *IEEE Trans. Signal Process.,* vol. 62, no. 4, pp. 939–953, Apr. 2014.

[25] H. M. Ozaktas, O. Arikan, M. A. Kutay, and G. Bozdagt, "Digital computation of the fractional Fourier transform," *IEEE Trans. Signal Process.,* vol. 44, no. 9, pp. 2141–2150, Sep. 1996.

[26] J. N. Briggs, *Target Detection by Marine Radar*. London, U.K.: Inst. Elect. Eng., 2004.

[27] S. Yan, H. Zhou, and J. Gong, "GNSS imaging: A case study of tree detection based on Beidou GEO satellites," *Prog. Electromagn. Res. C,* vol. 84, pp. 227–240, 2018.
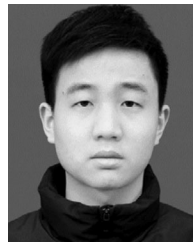
Yan Li received the B.Eng. degree in electronic information from the Shijiazhuang Tiedao University, Shijiazhuang, China, in 2018, and the M.A. degree in circuits and systems in 2021 from Wuhan University, Wuhan, China, where he is currently working toward the Ph.D. degree in electronic information with the School of Remote Sensing and Information Engineering.

His research interests include target detection and imaging with GNSS-based passive radar.

Songhua Yan received the Ph.D. degree in radio physics from the Wuhan University, Wuhan, China, in 2006.

He is currently an Associate Professor with the School of Remote Sensing and Information Engineering, Wuhan University. His research interests include radio communication, radar, and remote sensing.

Jianya Gong received the Ph.D. degree in photogrammetry and remote sensing from the Wuhan Technical University of Surveying and Mapping, Wuhan, China, in 1992.

He is currently a Professor with the School of Remote Sensing and Information Engineering, Wuhan University, Wuhan, China. He is an Academician of the Chinese Academy of Sciences, Beijing, China. His research interests include remote sensing image processing, spatial data infrastructure, and geospatial data sharing and interoperability.